Numerical simulation of a fracture toughness test of an Al6061-T6 aluminium alloy using a ductile criterion

Andrea Gilioli*, Andrea Manes, Marco Giglio

Politecnico di Milano, Department of Mechanical Engineering, Via La Masa 1, 20156 Milan, Italy

Article history:
Received 2 May 2013
Received in revised form 31 July 2013
Accepted 16 August 2013
Available online 5 September 2013

1. Introduction

In real components the possibility to have a pre-existing crack is generally not neglectable; the crack tip is characterized by a plastic zone with a very high gradient of strain. If such conditions have to be replicated by means of numerical models, that simulate ductile failure using damage criterion based on the accumulation of plastic strain, the attainment of reliable results is not straightforward. In the present research, an experimental campaign using cracked specimen has been carried out and simulated by means of a high fidelity numerical simulation (finite element model) in an explicit framework. C(T) specimens aimed to assess fracture toughness have been used. Fracture toughness is a quantitative parameter, which is related to the resistance of a material that has an inside crack. It is a property of the material and it can be obtained following the international standard (ASTM, 2013). The availability of such a standard allows a well-defined test and procedure.

Numerical models of C(T) specimens have been created and analyzed to replicate standard tests. These simulations exploit the Bao-Wierzbicki (BW) ductile damage criterion (Bao and Wierzbicki, 2004) previously calibrated using standard tensile tests on smooth and notched specimens and multiaxial tests (Gilioli et al., 2010). This kind of criterion is based on a phenomenological approach and its most important part regards the definition of a fracture locus: a relation between the plastic strain at failure and the triaxiality. The aim of the present research is therefore to verify, in a virtual test environment, the material calibration of Al6061-T6, obtained from Gilioli et al. (2010) in a different scenario (geometrical transferability). Thus a high fidelity numerical model of the C(T) specimens has been built and loaded to reproduce the experimental tests. Such investigation allows checking the geometrical transferability of the calibrated BW criterion even in state of strain dominated by large plasticity and a high strain gradient.

A further example of the calibration of a ductile damage criterion for Al6061-T6 can be found in Beese et al. (2010). Similar research publications regard the application of a BW model to reproduce slant fracture (Giglio et al., 2012a; Viganò et al., 2012). The authors have calibrated the mechanical behaviour of a titanium alloy and have subsequently exploited the calibration for the simulation of the slant fracture of a titanium helicopter main rotor hub. A good correlation between the experimental and numerical fracture shape, in particular regarding the first stage of the fracture path, has been demonstrated.

A complete and in depth overview of ductile fractures is reported in Li et al. (2011). Another inspiring paper is Xue and Wierzbicki (2008) where the authors have studied crack initiation and propagation in Al2024-T351 compact tension specimens and in a three point bending test. They have also applied the damage plasticity theory incorporating the pressure sensitivity and the Lode angle dependence into a nonlinear damage rule.

As highlighted in the literature, the application of a macroscopic failure criterion (BW) in a scenario where the stress (strain)

* Corresponding author. Tel.: +39 02 2399 8630; fax: +39 02 2399 8263.
E-mail address: andrea.gilioli@mail.polimi.it (A. Gilioli).

Table 1
Chemical composition of Al 6061-T6 section.

Al [%]	Mg [%]	Si [%]	Fe [%]	Cu [%]	Mn [%]	Cr [%]	Zn [%]	Ti [%]
98	0.8–1.2	0.4–0.8	0.7	0.15–0.4	0.15	0.04–0.35	0.25	0.15

gradient is very high, thus involving material at grain size, is of interest. A fracture toughness test is a significant scenario suitable for the investigation of this issue, being a very localized problem, due to the sharp crack defect. Aim of the present work is to analyze such effects with a discussion that includes also crystallographic analyses.

Mesh size dependence is a very interesting issue to investigate in current research framework. In Li and Karr (2008), Li et al. (2007) authors have developed a close form expression of the mesh-size and material dependent strain to failure by using the concept of strain bifurcation and in Li and Wierzbicki (2009) the mesh size effect is analyzed from a non-local point of view in applications based on a semi-coupled plasticity/damage theory. Another interesting work is Qian (2011), where the authors have studied crack extension using the Gurson-Tvergaard fracture approach in a computation cell approach for a steel. They underline that the typical in-plane length scale lies between 100 μm and 300 μm, and in the thickness direction the element size has to be less than or equal to the in-plane length scale, in order to predict a converged fracture resistance and crack front extensions.

2. Material Al6061-T6

The material that has been tested is an Al6061-T6 aluminium alloy. Generally speaking aluminium alloys have good mechanical properties, high corrosion strength and low density. Nowadays the fields of application of this kind of alloy are mainly the ones in which weight reduction is a critical factor, such as in aerospace applications, and in the field of transport in general. Al 6061-T6 belongs to the aluminium series 6000 with silicon and magnesium as the principal alloying components. The T6 suffix describes the heat treatment applied to the alloy, T6 stands for a two phase treatment. The entire process is based upon the precipitation hardening phenomenon and it results in a larger increment in strength with only a minimal reduction of the break elongation. Table 1 summarizes the main physical-chemical properties of Al 6061-T6 (Qian, 2011).

3. C(T) experimental tests

Fracture toughness experiments on compact test (C(T)) specimens have been performed on a hydraulic MTS 810 machine with a load cell of 100KN. The same machine has been used to pre-crack the specimens and all the tests have been carried out according to (ASTM, 2013). Complying with the standard, a specimen has been, in a first stage properly pre-cracked by means of fatigue cycles, and subsequently an increasing displacement has been applied to break it. To reach the desired pre-crack length, which is around 7.11 mm (the average value of all the tested specimen), about 30,310 load cycles and a maximum load of 22KN is needed. A drawing of the C(T) specimens is shown in Fig. 1(a). Also the specimens with side grooves, consisting of a cut with a triangular profile on each side, have been considered. The side grooves opening angle is 61°. The thickness of both kinds of specimens is 25.4 mm. Load versus the extensometer displacement curves have been acquired. For both specimens the extensometer has been placed at the knife-edge location. Two tests have been carried out for the C(T) plain shape specimen geometry and 1 test for the C(T) specimen with side grooves. The experimental load/displacement curves are shown in Fig. 5. The P_{max}/P_Q ratio is around 1.30, which does not satisfy the standard requirement to achieve the linear elastic plane strain fracture toughness (ASTM, 2013). Nevertheless, this is not a relevant issue in the present research because the main goal is not to determine the linear elastic plane strain fracture toughness, K_{IC}, but rather to investigate the behaviour of the numerical model in presence of both a relatively large plastic zone and high strain gradients. The C(T) test is a very representative "environment" where these conditions are dominant. Thus load displacement curves are the main output from the experimental tests.

4. FE model

Finite element models of the fracture toughness experimental tests have been performed (both for the plain shaped and side-grooved specimens). The models have been built using the commercial software ABAQUS 6.12 in an explicit framework. The Explicit solver allows the handling of the numerical analysis which involves large plasticity and non-linearity. In order to reproduce the real conditions two reference points have been created: one in the centre of each hole. These reference points are connected to the internal surface of the hole, using a coupling kinematic constraint. For the upper hole a constrain has been chosen which allows rotation, but among the various displacements, only vertical one is allowed. For the lower hole a constrain which allows rotations but keeps all the other displacements fixed, has been chosen, as shown in Fig. 2a. In order to simulate the real load distribution due to contact, only half of the inner surface of each hole has been coupled with the corresponding reference point. Finally in the upper hole a vertical displacement has been defined. Its value reproduces the displacement applied to the specimens during the experimental tests. The models have been developed using C3D8R, 3D solid elements with a reduced integration. The pre-crack has

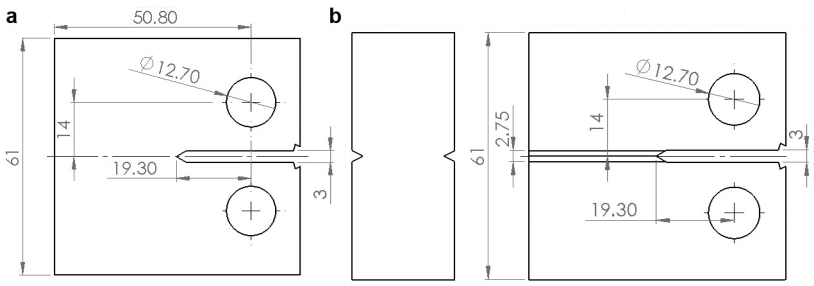

Fig. 1. Experimental C(T) specimen (a) plain shaped; (b) side-grooved.

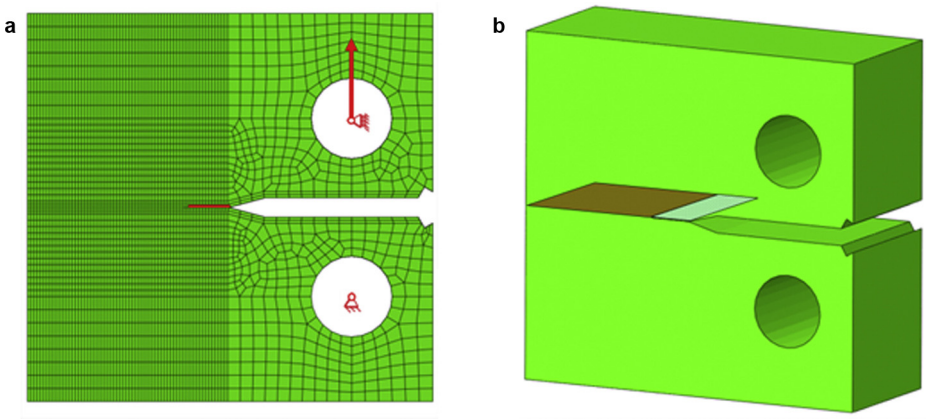

Fig. 2. (a) Numerical model with constrains. (b) Numerical model with the resistance area which fails due to the fracture toughness test highlighted (red) and seam (pre-cracked area) hatched. (For interpretation of the references to color in this figure legend, the reader is referred to the web version of the article.)

Table 2
Johnson-Cook material parameters.

A_{JC} [MPa]	B_{JC} [MPa]	n_{JC}
270.0	154.3	0.2215

been reproduced using an ABAQUS feature called "seam" which allows the creating of a cut inside a mesh, splitting nodes along a line (hatched area in Fig. 2b). The pre-crack length is identical to the average experimental one and is around 7.11 mm long.

Analyses with different mesh sizes for the elements in the fracture area (red region in Fig. 2b) have been investigated. The model total number of elements is: 706,656 for a 0.25 mm mesh, 174,050 for a 0.5 mm mesh and 49,790 for a 1 mm mesh. Proper mesh refinements have been built in order to avoid severe variation of the mesh size in area subject to failure.

The material calibration has been carried out in previous research (Gilioli et al., 2010) in which a characterization of the mechanical behaviour of Al6061-T6 was studied. The material constitutive law is a Johnson-Cook (neglecting the strain rate and the temperature effect), see Eq. (1). In Table 2, the JC material parameters are summarized: A_{JC} is the onset of the yield while B_{JC} and n_{JC} describe the hardening slope.

$$\sigma = A_{JC} + B_{JC}(\varepsilon_{pl})^{n_{JC}} \tag{1}$$

Regarding fracture, a Bao-Wierzbicki ductile damage criterion has been adopted. This phenomenological approach has been chosen due to the fact that it allows the description of the failure onset at different stress triaxiality with good accuracy and reduced computational efforts. The ductile failure criterion adopted is assumed to be uncoupled from the constitutive model. The core of the model is the curve which describes strain at the failure as a function of stress triaxiality (Bao and Wierzbicki, 2004). This curve has been calibrated in Gilioli et al. (2010) by means of experimental tests on simple specimens (with different loading conditions) replicated by means of numerical simulations in order to track the development of stress and strain at the critical sites until fracture. The result is a "multi branch" strain at a failure function that fits the experimental material damage behaviour (Bao and Wierzbicki, 2004). For negative triaxiality a vertical asymptote for a value of −1/3, the so called cut-off value, is present. For this type of condition, there is no fracture. There is a minimum of the fracture locus at zero triaxiality (pure shear). The curve increases in the region from zero to around 1/3 and then decreases monotonically with a horizontal asymptote around zero. All the parameters (for the several branches), taken from Gilioli et al. (2010), are reported in Table 3.

5. Mesh size effect on fracture

Ductile damage criteria are based on the accumulation of plastic strain. When the cumulative plastic strain for an element reaches a critical value, the element suddenly fails and completely loses its load-carrying capability (failed elements and related nodes are therefore removed from the analysis). The accumulation of strain is weighted by a function, the so called fracture locus, described in the previous section. This curve for a BW fracture model describes the relation between stress triaxiality and plastic strain at failure. It is thus possible to define a damage variable D, see Eq. (2); when its value reaches a conventional value (equal to 1) the corresponding element is deleted.

$$D = \int_0^{\bar{\varepsilon}_f} \frac{d\varepsilon_{pl}}{\varepsilon_f(\eta, \bar{\vartheta}, \dot{\varepsilon}_{pl}, T)} \tag{2}$$

The denominator of Eq. (2) is the fracture locus function, which potentially depends on a number of variables (such as triaxiality, Lode angle, strain rate, and temperature). With D calculated for each element, the mesh dependence in a fracture simulation becomes evidently the key issue especially in the presence of high gradients in the stress and strain pattern. Finite element methods divide the real material continuum in elements, evaluating only values of the stress/strain condition (gradient) in each element with a well-defined internal function. This means that if an element is not small enough, the calculated strain fails to follow a high gradient and thus fails to be representative of the real situation resulting in a numerical tendency of the element to fail later because the evaluated damage on the whole element is potentially less than expected.

Table 3
Bao-Wierzbicki material parameters (Gilioli et al., 2010).

Stress triaxiality η	$\eta_{av} < 0$		$0 < \eta_{av} < 0.0223$		$0.0223 < \eta_{av} < 0.0626$		$0.062 < \eta_{av} < 0.37$		$\eta_{av} > 0.37$	
Equation	$\varepsilon_f = \frac{A}{\eta+1/3} - 3A + \varepsilon_{ftp}$		$\varepsilon_f = m \cdot \eta + q$		$\varepsilon_f = m \cdot \eta + q$		$\varepsilon_f = m \cdot \eta + q$		$\varepsilon_f = \frac{A}{\eta}$	
Coefficients	**A**	0.428	**m**	20.85	**m**	−5.43	**m**	−0.848	**A**	0.17
	ε_{ftp}	0.474	**q**	0.474	**q**	1.060	**q**	0.774		

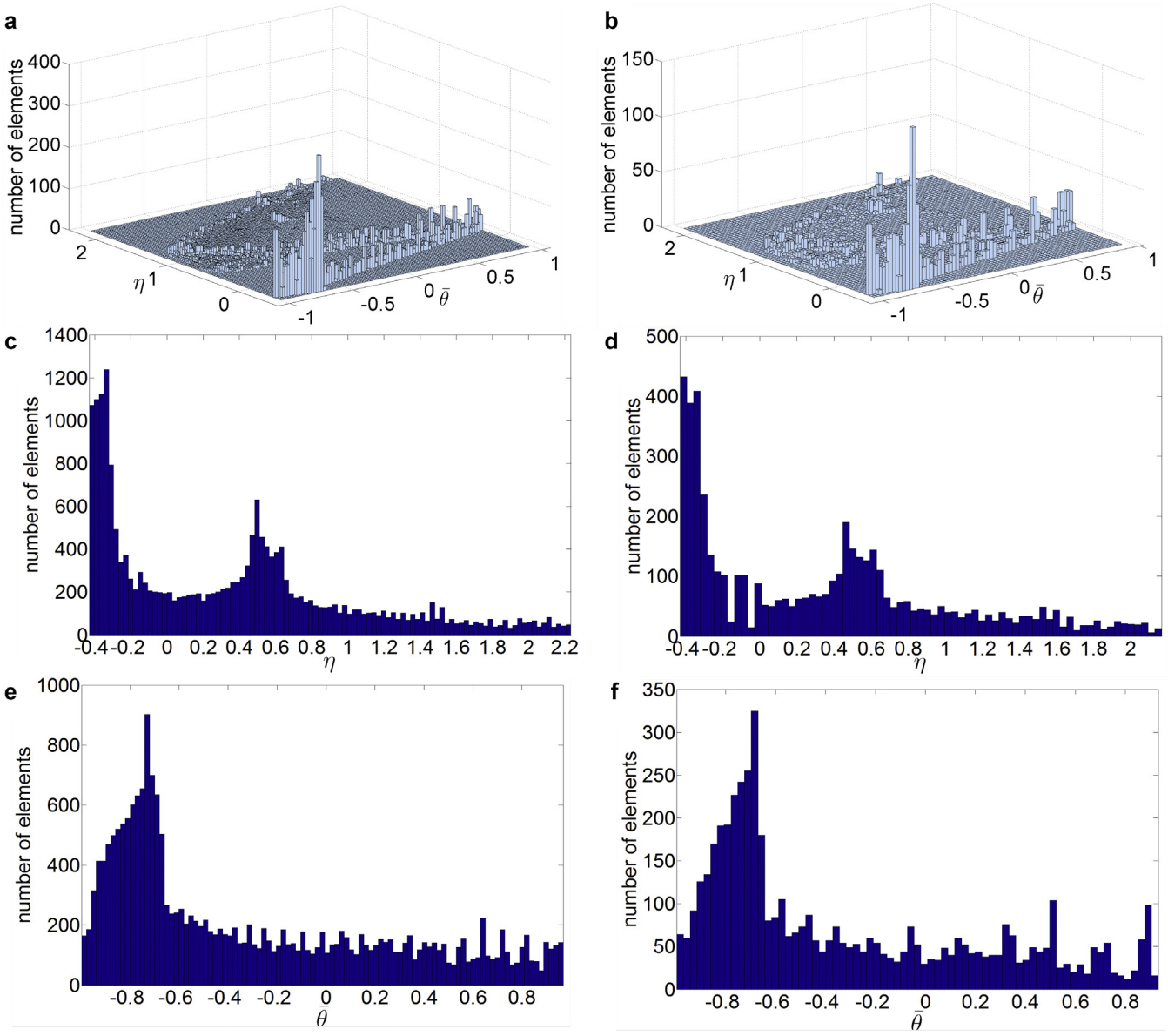

Fig. 3. Histogram representing the number of elements with a certain stress state (triaxiality, Lode angle) at the onset of the fracture for different mesh sizes (a–c–e) 0.25 mm and (b–d–f) 0.5 mm.

Instead, in a very refined mesh, failure happens earlier because it is easier to find an element which is small enough to completely include only a damaged zone. A severe strain gradient generated at the crack tip, like in the C(T), is therefore an interesting test to assess the robustness of the criterion. In order to investigate such behaviour in detail, first of all two different analyses with different mesh sizes, but without considering damage (no crack is present), have been carried out. The idea is to evaluate the stress state at the onset of the fracture using a different mesh size. Fig. 3(a) and (b) describes the stress state in terms of numbers of elements that have a certain value of Lode angle and triaxiality and it is thus a summary map of the load condition for the plane shape component. Lode angle and triaxiality are two parameters which can effectively summarize the stress state. According to Beese et al. (2010) triaxiality, η, can be calculated as Eq. (3) and the so called Lode angle parameter, $\bar{\vartheta}$ as Eq. (4). Remembering that ζ (normalized third stress invariant) can be calculated as Eq. (5):

$$\eta = \frac{\sigma_h}{\sigma_{VM}} \tag{3}$$

$$\bar{\vartheta} = 1 - \arccos\frac{\zeta}{\pi} \tag{4}$$

$$\xi = \left(\frac{r}{q}\right)^3 \tag{5}$$

where r is the third invariant and q is the second one (of the stress tensor).

The base size of each column section in Fig. 3 is about the size of the adopted mesh element, therefore in Fig. 3(a) the base size is about 0.25 mm and in Fig. 3(b) it is about 0.5 mm. The most important conclusion can be drawn from Fig. 3, which shows that there is no relevant difference in the stress distribution over the entire surface regardless of the mesh size. It is clear that moving to a coarser mesh the height of the columns and their number decrease because there are in total less elements but the general distribution of triaxiality and Lode angle over the mesh grid is very similar. The analysis of Fig. 3(c)–(f) clearly indicates the overall similarity in the two cases. In these figures the 3d histogram is plotted showing the trend of triaxiality and Lode angle separately.

Table 4
Mean and variance for the triaxiality data for two different mesh sizes.

Mesh 0.25 mm	Mesh 0.5 mm	Perceptual difference
Triaxiality: mean		
0.337	0.328	2.7
Triaxiality: variance		
0.455	0.45	1.1

Table 5
Mean and variance for the Lode angle data for two different mesh sizes.

Mesh 0.25 mm	Mesh 0.5 mm	Perceptual difference
Lode angle: mean		
−0.311	−0.318	2.2
Lode angle: variance		
0.315	0.295	6.7

Again the similarity for both meshes is evident. A final quantitative comparison is described in Tables 4 and 5. The mean and the variance of the Lode angle and triaxiality data have been elaborated. Comparing these datasets regarding the two different meshes the perceptual difference is always less than 7% demonstrating again the similarity of the two cases.

Fig. 3 gives an overview of the stress state in all of the fracture surfaces and provides an overall knowledge of the load condition, whereas Fig. 4 provides a detailed analysis of the stress/strain condition around the crack tip (thus considering the crack in the model). For the BW ductile damage fracture the two most important parameters to evaluate are stress triaxiality and the equivalent plastic strain (PEEQ). Fig. 4(a) and (c) show triaxiality and the PEEQ along the crack profile at the onset of failure referring to the numerical analysis with a 0.25 mm mesh size, instead Fig. 4(b) and (d) refer to a 0.5 mm mesh. Not only the results along the crack border are plotted, but also triaxiality and the PEEQ are evaluated even at a distance of 0.25 mm and 0.5 mm from the pre-crack tip. In case of a 0.5 mm mesh, only a distance of 0.5 mm ahead of the crack tip has been evaluated. A comparison of the results of the two different meshes, shown in Fig. 4, leads to relevant conclusions. First of all the triaxiality appears unaffected in a significant way by mesh size. There is a slight effect along the crack border, but at a distance of 0.5 mm from the crack tip, the triaxiality value has no significant variation. However, the evaluation of the PEEQ, which is the real driving parameter of fracture, is of greater importance. Far from the crack tip (0.5 mm) there is an almost reduced plastic strain for both the refined and coarse mesh. Instead, along the crack tip border in case of a mesh of 0.25 mm, plastic strain is much higher (about twice as high) than in the case of the coarse mesh. In both cases, the numerical models show a reasonable trend for plastic strain, which is higher in the centre of the specimen (plane strain) rather than at its external sides. The similarity of the results at just 0.5 mm from the crack tip indicates that the failure of pre-cracked C(T) specimen is very localized and hence is largely prone to mesh effect issues.

Fig. 5 shows the effect of the mesh size on the numerical load–displacement curves. It is evident that reducing the mesh size results in failure at lower displacement but without an asymptotic value at which the results converge. A continuous decrease of the mesh size leads to a diverging of the results after a certain element dimension. The mesh size, which provides the highest similarity between the numerical model and the experimental results, lies between the lower limit of 0.1 mm and the upper limit of 0.25 mm. The same conclusion can be drawn for the C(T) specimen with side grooves, see Fig. 5(b). The numerical model is able to reproduce in a satisfactory way the experimental curves in particular as far as global stiffness of the specimens and their behaviour prior to failure are concerned. It is interesting to remark that the mesh size effect regards only the peak load estimation and not the model stiffness.

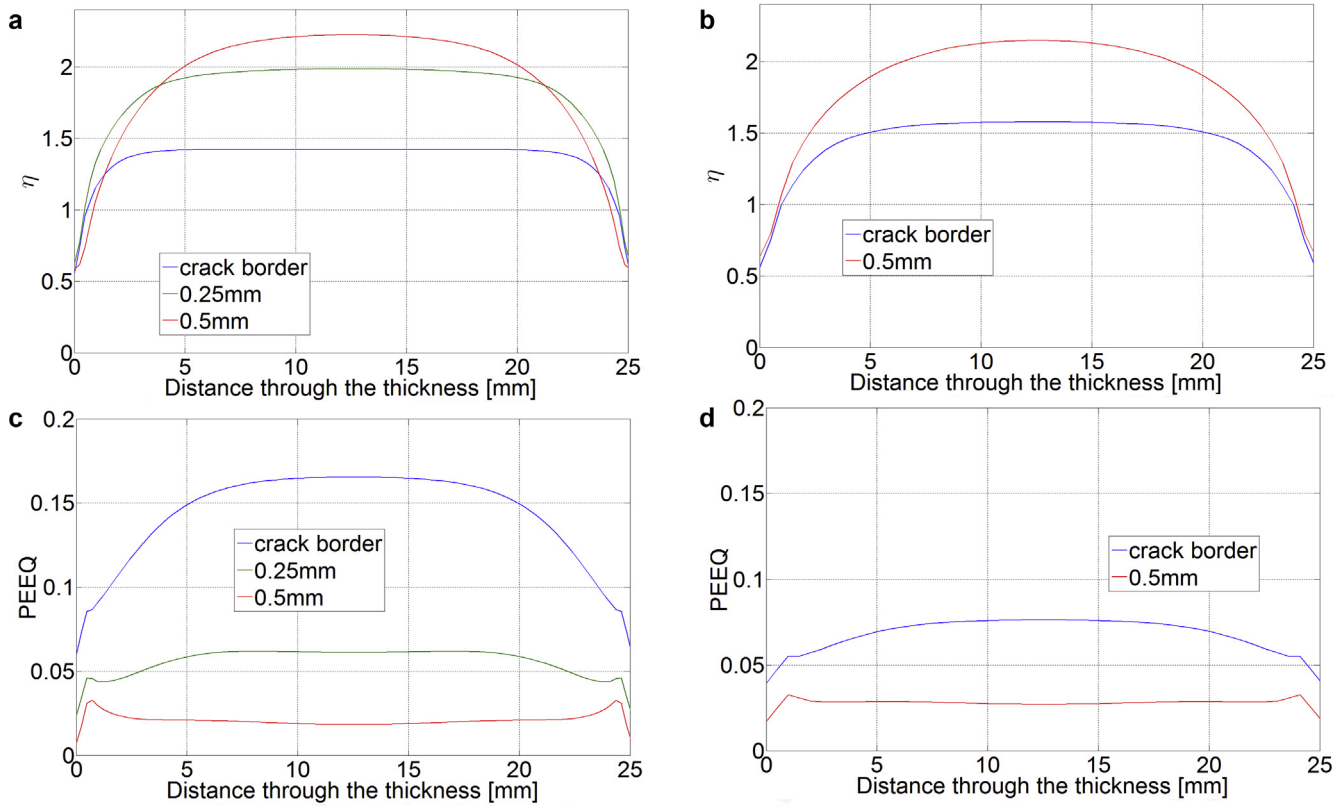

Fig. 4. Triaxiality, (a–b), and equivalent plastic strain, (c–d), along a path through the specimen thickness at various distances from the crack front – (a–c) mesh 0.25 mm; (b–d) mesh 0.5 mm.

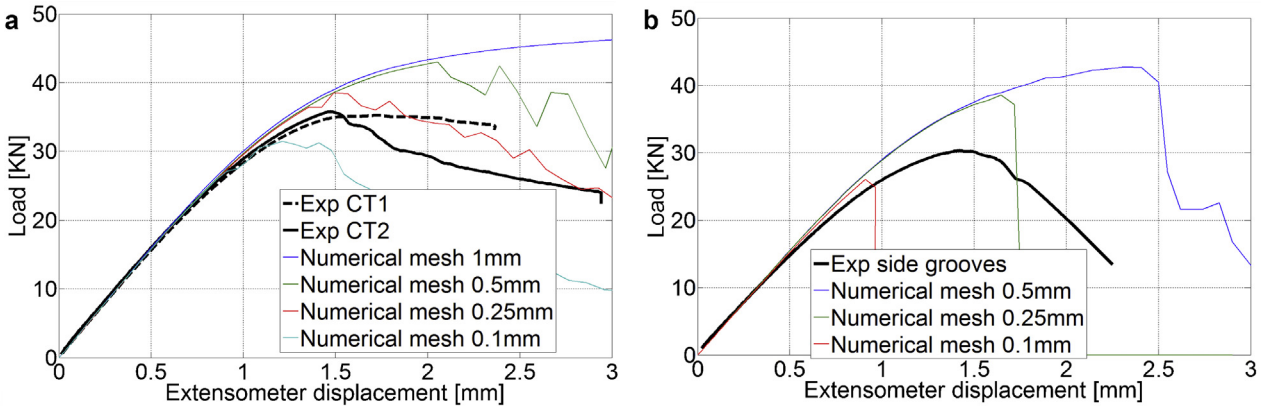

Fig. 5. Comparison between the load–displacement curve for a classic C(T) specimen (a) and for a specimen with side grooves (b).

Independent of the mesh size is adopted, the undamaged estimated stiffness of the specimen is always the same and this value is very close to the experimental one.

In Table 6, a quantitative estimation of the error on the evaluation of the peak load between the numerical model and the average value form the experimental curves is summarized (the 1 mm mesh is neglected due to the lack of a reasonable maximum load value achieved in the simulated displacement range).

The effect of the mesh size has been further analyzed in a different scenario, which is the tensile test on round smooth specimen. A description of the experimental set up can be found in (Gilioli et al., 2010) where the authors carried out a study in order to calibrate the mechanical behaviour of an Al6061-T6 aluminium alloy. In the present paper a high fidelity numerical approach has been followed to numerically reproduce the experimental tensile test on round specimen exploiting the experimental data from Gilioli et al. (2010). In particular the effect of different mesh sizes on the results has been focused on. Fig. 6 shows the mesh effect on the tensile test. It is important to underline that decreasing the mesh size results in a reduction of the displacement at failure, but with a much lower effect compared with the fracture toughness test. The other relevant aspect regards the optimal mesh size that in this case seems to be higher than 0.75 mm. Actually due to the calibration, procedure adopted from Gilioli et al. (2010) the fracture toughness simulation test and the tensile test cannot be directly compared. Indeed the latter has been used for the calibration while the first one has been used for the validation. The only conclusion that can be drawn, looking at Fig. 6, regards the suitability of the fracture model that is largely verified and the reduction of the displacement at failure due to the decrease of the mesh size. The different load scenarios in terms of loading condition between the fracture toughness and tensile test are important factors to consider.

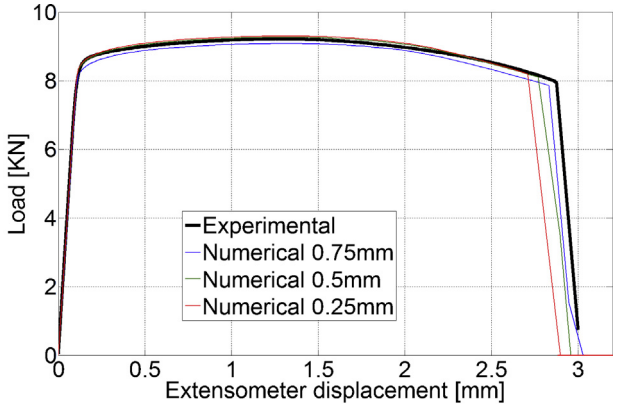

Fig. 6. Comparison between the numerical and experimental load/displacement curve for the tension test of a round smooth specimen.

6. Aluminium 6061-T6 microstructure

In order to find a possible connection between the optimal mesh size and some physical material aspects, the microstructure of Al6061-T6 has been analyzed following the procedure suggested in ASM (1992) which was previously used by the same authors (Giglio et al., 2012b; Mapelli et al., 2011). First of all a small specimen of the dimension of about 20 mm × 20 mm × 10 mm is cut from a tested C(T) specimen. The surface of the new specimen is then accurately mirror polished to make it suitable for the subsequent electrolytic etching. The procedure is based on the different tendency of material crystal components to corrode and thus the electrolytic etching can highlight the microstructure. In the electrolytic etching, the tested specimen acts as the anode while a steel bar is the cathode. In order to complete the electrolytic cell a Barker's reagent is needed. This composed of 4–5 mL HBF_4 (48%) and 200 mL of H_2O. To avoid over-etching of the surface, the electrolytic etching is carried out in following steps of 100 s each. After the etching, the microstructure is analyzed using an optical microscope with polarized light. In Fig. 7, the Al6061-T6 microstructure is reported. The black points are the corrosion pits caused by the excessive exposure to the chemical etching agent. The grain size and shape analysis are of particular interest. The shape analysis shows that the grains are

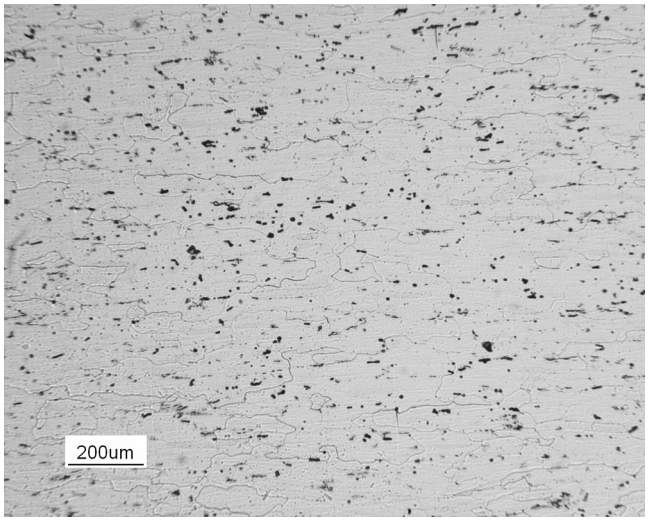

Fig. 7. Al6061-T6 microstructure, obtained after electrochemical polishing.

Table 6
Error on the peak load estimation.

C(T) specimen		C(T) specimen with side grooves	
Mesh size [mm]	Error on peak load [%]	Mesh size [mm]	Error on peak load [%]
0.5	20.4	0.5	41.5
0.25	7.3	0.25	28.2
0.1	−11.7	0.1	−13.6

slightly stretched in the rolling direction demonstrating that the original thick plate, from which the specimen have been cut, was gently rolled to reduce its thickness. Fig. 7 shows that the grains vary in shape and size but exhibit an overall approximate rectangular shape. The horizontal dimension, according with Fig. 7, is the longest one and its average length lies between around 0.2 mm and 0.6 mm, whereas the vertical dimension is always the shortest one with values ranging from 0.05 mm to 0.2 mm. The interval, representing the smallest size of elements, is almost identical to the optimal mesh (0.1–0.25 mm) demonstrating that the best mesh size should be chosen according to the microstructure of the material.

Scanning electron microscopic images have been taken, as shown in Fig. 8, to provide a detailed analysis of the fracture surface. As expected the fracture surface is very different between the pre-cracked area and the final surface after failure, due to the different failure behaviour, see Fig. 8(a): crack propagation in the pre-cracked region (hatched area in Fig. 3(b)) and the slant fracture for the remaining area, red area in Fig. 3(b)). Two different points have been analyzed in the failure region caused by the fracture toughness test. One point is close to the border with the pre-cracked area (the region inside the static failure section), see Fig. 8(b)–(c)) and one point lies around the centre of the static failure region, see Fig. 7(d) and (e)). For both points, two magnifications of 150× and 1000× have been used. The failure is clearly ductile due to the presence of many evident dimples but at the same time many several brittle areas are present. The point far from the border exhibits less dimples with an apparent reduction of ductility.

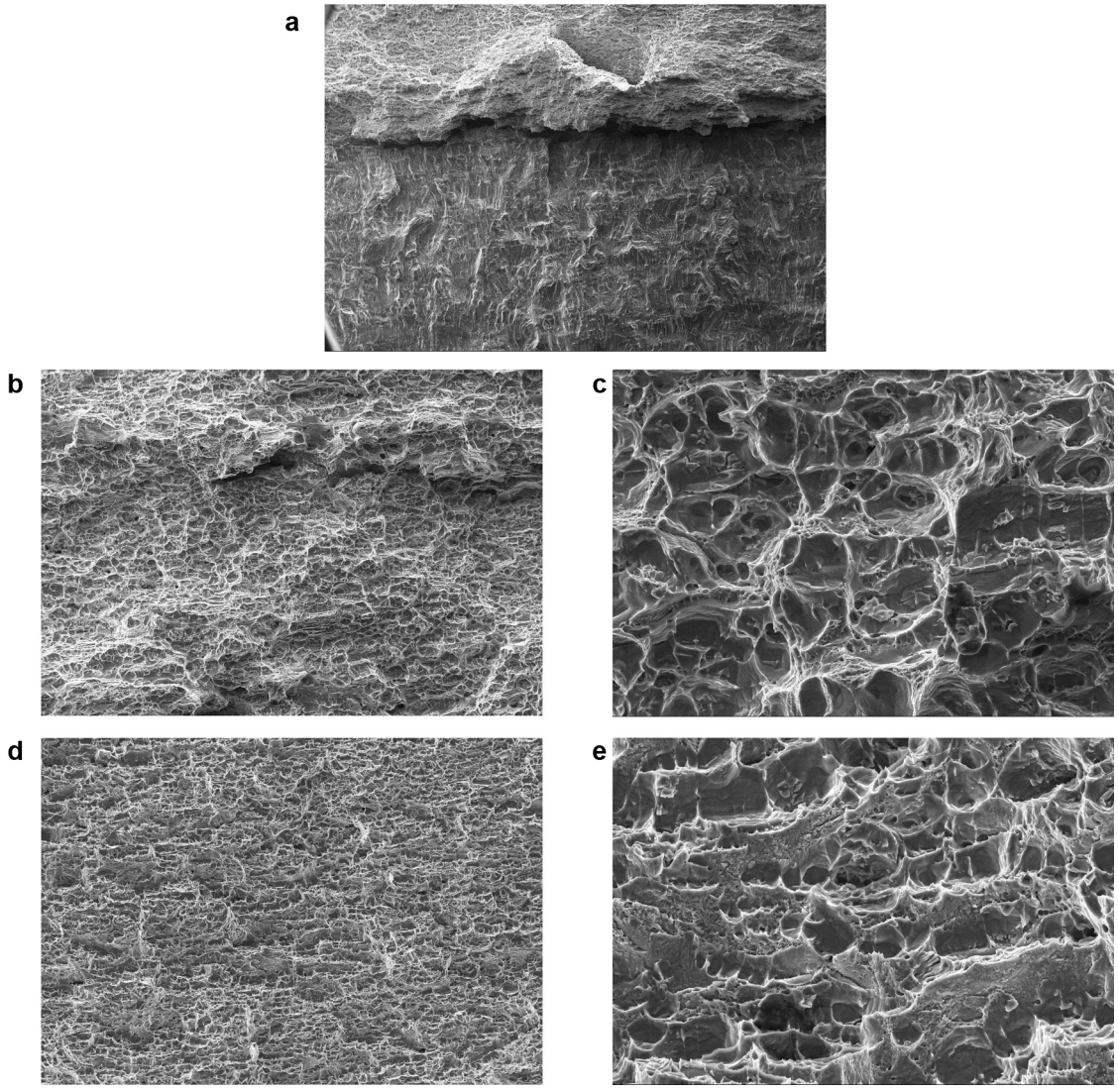

Fig. 8. SEM pictures of the fracture surface. (a) 50× comparison between the pre-cracked area (lower part) and the final failed area, (b–c) 150–1000× area close to the border of pre-cracked region but inside the failure section, (d–e) 150–1000× area far from the border of pre-cracked region inside the fracture.

7. Conclusion

The main goal of the present paper is to exploit the calibration of a phenomenological ductile damage criterion (BW) in a different scenario in order to check the geometrical transferability even in state of strain dominated by a high strain gradient. When a substantial strain gradient is present, mesh size can be an issue for the damage criterion, which is based on the accumulation of the PEEQ. The material calibration of Al6061-T6 aluminium alloy has been obtained in previous research based on the application of the reverse method to reproduce uni and multi-axial tests. Exploiting this calibration, a Johnson-Cook constitutive law and a Bao-Wierzbicki ductile fracture criterion have been adopted in the present research to investigate the possibility to reproduce with good similarity a fracture toughness test with C(T) specimen. Such specimens and test procedures have been chosen because they are not only well-defined test procedures but are moreover representative of the state of strain dominated by a high strain gradient. Within this framework relevant and critical aspects of the problem have been studied. In particular the mesh size effect has been shown to play a crucial role into the reproduction of failure. The size of the elements strongly affects the estimation of the critical maximum load but it has almost no effect prior the fracture onset. The developed numerical model is able to reproduce the initial elastic behaviour of the specimen well, independent of the element size that has been adopted. Only when the plastic strain becomes relevant (approaching fracture) the mesh size plays a very important role. A reduction of the mesh size results in failure at lower displacement (load) but without an asymptotic value at which the results converge. A continuous decrement of the mesh size leads to diverging results. The two quantities, which control failure according to the phenomenological ductile damage criterion investigated are: triaxiality and the equivalent plastic strain (PEEQ). Their behaviour depending on mesh size has also been investigated. Triaxiality is almost unaffected by the element size but the PEEQ increases significantly in a small area along the crack tip border adopting a refined mesh rather than a coarse one. In order to find a possible physical explanation of the mesh size effect, a combined approach between the study of the microstructure of the material and parametric numerical analysis with different mesh dimensions has been developed. Results show that there is an optimal element dimension, which leads to the best similarity between the numerical and the experimental load-displacement curves. This dimension has been found to be very close to the grain dimension of the 6061-T6 measured by means of microstructure investigations. Thus the present research highlights the need for a physical choice of the right mesh dimension (related to the dimension of the material grain) when a severe strain gradient is present. The drawn conclusions are valid for both the two different geometries of the C(T) specimen: with and without side grooves. The element size seems to affect in the same way the numerical load/displacement curves for both configurations.

References

. ASM Handbook Committee – Metallography and microstructures, vol. 9.

2013. ASTM E1820 Standard Test Method for Measurement of Fracture Toughness.

Bao, Y., Wierzbicki, T., 2004. A comparative study on various ductile crack formation criteria. Journal of Engineering Materials and Technology 126 (3), 314–324.

Beese, A.M., Luo, M., Li, Y., Bai, Y., Wierzbicki, T., 2010. Partially coupled anisotropic fracture model for aluminum sheets. Engineering Fracture Mechanics 77, 1128–1152.

Giglio, M., Manes, A., Viganò, F., 2012a. Ductile fracture locus of Ti–6Al–4V titanium alloy. International Journal of Mechanical Sciences 54, 121–135.

Giglio, M., Manes, A., Mapelli, C., Mombelli, D., Baldizzone, C., Gruttadauria, A., 2012b. Crystallographic analysis of specimens used for calibrate a failure model for an Al 6061–T6 alloy. Key Engineering Materials 488–489, 89–92.

Gilioli, A., Manes, A., Giglio, M., 2010. Calibration of a constitutive material model for Al 6061-T6 aluminium alloy. In: 4th International Conference on Advanced Computational Engineering and Experimenting, ACE-X 2010, Paris, France, 8 and 9 July.

Li, Y., Karr, D.G., 2008. Prediction of ductile fracture in tension by bifurcation, localization, and imperfection analysis. International Journal of Plasticity.

Li, Y., Wierzbicki, T., 2009. 2009 Mesh-size Effect Study of Ductile Fracture by Non-local Approach. In: Proceedings of the SEM Annual Conference June 1–4, Albuquerque, NM, USA.

Li, Y.N., Karr, D.G., Wang, G., 2007. Mesh size effects in simulating ductile fracture of metals. In: 10th International Symposium on Practical Design of Ships and Other Floating Structures, Houston, TX, United States of America.

Li, H., Fu, M.W., Lu, J., Yang, H., 2011. Ductile fracture: experiments and computations. International Journal of Plasticity 27, 147–180.

Mapelli, C., Manes, A., Giglio, M., Mombelli, D., Baldizzone, C., Gruttadauria, A., 2011. Microstructural investigation on an Al 6061 T6 alloy subjected to ballistic impact. Procedia Engineering 10, 3447–3452.

Qian, X., 2011. An out-of-plane length scale for ductile crack extensions in 3-D SSY models for X65 pipeline materials. International Journal of Fracture V167, 245–269.

Viganò, F., Manes, A., Giglio, M., 2012. Numerical simulation of the slant fracture of a helicopter's rotor hub with a ductile damage failure criteria. Fatigue and Fracture of Engineering Materials and Structures 35 (4), 317–327.

Xue, L., Wierzbicki, T., 2008. 2008 Ductile fracture initiation and propagation modeling using damage plasticity theory. Engineering Fracture Mechanics 75, 3276–3293.